Hydrothermal optimisation of hybrid nanoparticle mixture fluid flow in a porous enclosure under a magnetic field and thermal radiation

MAYSAM ZABETI[1], JAHANFAR KHALEGHINIA[1,*], BAHRAM JAFARI[2] and MORTEZA MOHAMMADI[1]

[1]Department of Mechanical Engineering, Nour Branch, Islamic Azad University, Nour, Iran
[2]Faculty of Engineering Modern Technologies, Amol University of Special Modern Technologies (AUSMT), Amol, Iran
*Corresponding author. E-mail: j.khaleghinia@gmail.com

Abstract. Fluid cavities have important integral roles in different engineering systems. However, a significant challenge is created by the natural convection (NC) within these cavities. Hence, the present work aimed to assess the heat transfer (HT) and fluid flow within a porous medium. For this purpose, a base fluid (f) was chosen comprising a 50–50 mixture of water–ethylene glycol. Moreover, by incorporating $TiO_2-Al_2O_3$ hybrid nanoparticles (HNP) into the base fluid, their effect on the HT processes and flow was explored. Primarily, the governing equations were derived by considering momentum, continuity and energy equations. Then, similarity solutions were utilised to convert partial differential equations (PDEs) for the flow and energy functions into ordinary differential equations (ODEs). Then, the problem was solved by considering the boundary conditions. To solve the ODEs, the non-commercial software Flex PDE was used through the numerical solution and finite element discretisation methods. Moreover, in the present work, optimal values were used to determine the response surface method (RSM). According to the results, an upward trend was presented by the temperature (T) profile with a decrementation in the electromagnetic intensity and porosity level. Moreover, the temperature profile was not significantly affected by increasing the radiation parameter (Rd).

1. Introduction

Natural convection (NC) is a fundamental method for heat transfer (HT) that represents the heat displacement between the mobile fluid and the surface with different temperatures. There are two main objectives for studying this phenomenon: comprehending the physical mechanisms and considering the calculation approaches. In HT enhancement, various shapes and novel materials have helped many researchers. For instance, a porous medium with vast applications contains a solid network connected by empty pores or spaces. Furthermore, adding solid materials with nanometer dimensions is among the solutions that have attracted significant attention. With higher thermal conductivity, such materials improve HT in various thermal systems.

Walker and Homsy [1] primarily studied NC in a cavity in this regard. Hussein and Mustafa [2] investigated NC in a fully open parallelogram cavity for the first time by using water as the base fluid and copper nanoparticles. It was revealed that by increasing the volume fraction and Rayleigh number (Ra) of the nanoparticles, the average Nusselt number (Nu) is increased. Parvin and Akter [3] examined the impact of magnetic parameters on NC HT in a prismatic enclosure with an uneven temperature distribution on the bottom wall. They revealed a direct relation between the Hartmann number (Ha) and temperature while observing an inverse relation to velocity variation. Sivaraj and Sheremet [4] quantitatively studied the NC HT in a porous medium with downward slopes and a solid heater in the middle. They found that non-linear changes in the
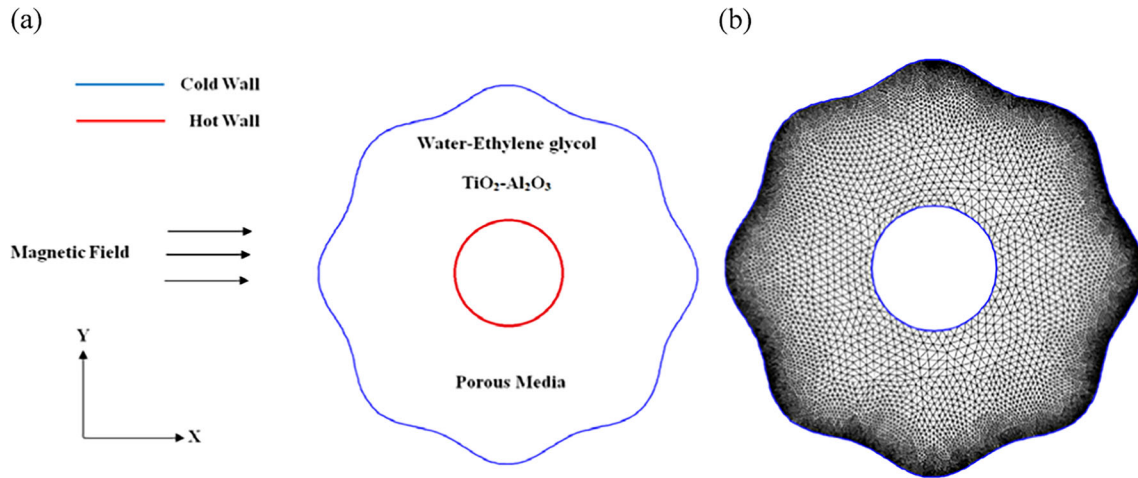
(a)   (b)

Figure 1. (**a**) The geometry and boundary conditions and (**b**) adaptive mesh refinement.

average Nusselt number (*Nu*) are caused by incrementing the applied magnetic field (*B*) angle.

Motlagh and Soltanipour [5] used the non-homogeneous two-phase Buongiorno's model to assess the NC HT within an inclined square cavity. According to their findings, the average Nusselt number (*Nu*) remains almost constant at low Rayleigh number (*Ra*), with the increase of the slope angle, regardless of the volume fraction of the nanoparticles. Janagi *et al* [6] identified the NC flow and HT of cold water in a square porous cavity. They revealed that by increasing the Darcy number and porosity increases the HT rate. The effect of the baffle on NC HT in a C-shaped cavity with a magnetic field was quantitatively evaluated by Abedini *et al* [7]. Their simulations indicated that by increasing the cavity dimensions ratio, *Nu* increases. Forced convection HT of water–copper nanofluid was assessed by Hassanpour *et al* [8] through a magnetic field using the finite volume method. Rashad *et al* [9] investigated the effect of the location and size of the heat source and heat sink on entropy generation and NC HT in a sloping porous cavity. It was revealed that by increasing the volume fraction of nanofluids, the entropy generation reduces, thus decreasing the irreversibility of HT.

Salari *et al* [10] numerically simulated the NC of two immiscible fluids within a rectangular container utilising aluminium oxide nanofluid and water. NC HT was examined by Ahmed *et al* [11] for two porous finned triangular cavities under a magnetic field. Copper was used as the nanoparticle and water as the base fluid. They also considered Darcy's model for the porous media. Alnaqi *et al* [12] quantitatively investigated the effects of magnetic field and radiation on the nanofluid-generated entropy and HT rate in a diagonal square cavity with conductive fins. They revealed

Table 1. The thermo-physical features of ethylene glycol–water and hybrid nanoparticles [29,30].

Physical properties	Ethylene glycol–water (50/50)	Al_2O_3	TiO_2
$\rho\left(\frac{kg}{m^3}\right)$	1063.8	3970	4250
$c_p\left(\frac{J}{kg \cdot K}\right)$	3630	765	686.2
$k\left(\frac{W}{m \cdot K}\right)$	0.387	40	8.95
$\beta \times 10^{-5}(k^{-1})$	58	10×10^{-10}	0.9

that by addition of nanofluid with a concentration of 6% in the absence of radiation results in an HT rate increase by about 5.9% and entropy generation by 16.6%.

Yu *et al* [13] studied the HT of molten salt and SiO_2 nanoparticles within a cylindrical cavity was simultaneously using experimental and numerical approaches. Moreover, Dogonchi *et al* [14] assessed the effect of nanoparticles' shape numerically on NC HT in a square-shaped porous medium with an oval-shaped cavity. Geridonmez *et al* [15] studied the MHD water–Al_2O_3 nanofluid flow numerically under a heater. They found that by increasing the heater's length, *Ra* and nanoparticle concentration, the HT rate increases. Dogonchi *et al* [16] used the finite element approach to examine the MHD NC of water–copper fluid in a square chamber using a wavy circular heater. Sadeghi *et al* [17] numerically investigated NC HT of the water as the base fluid and Al_2O_3 as nanoparticles using the finite element technique in a chamber with innovative
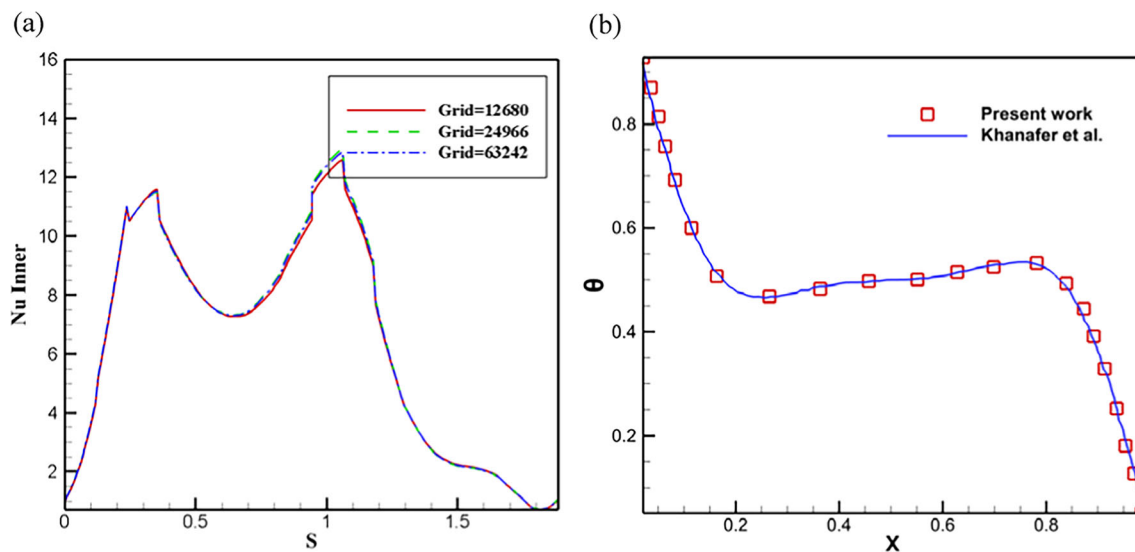
(a)

(b)

Figure 2. (**a**) The comparison of Nu_{Loc} for various grid sizes when $Ra = 200$, $Ha = 10$, $Rd = 0.5$, $\varepsilon = 0.7$ and (**b**) the validation of ongoing study with Khanfar *et al* [31]. $\phi = 0.01$ and $Pr = 6.2$ (Cu–water).

Table 2. The variation of different parameters in this study.

Working fluid	Porosity parameter	Hartmann number	Rayleigh number	Radiation parameter
Water–ethylene glycol	0.5 – 0.7 – 0.9	0 – 10 – 20	100 – 200 – 300	0 – 0.5 – 1

geometry and a wavy wall such as a trapezoidal heater. They observed that the highest HT rate was achieved with a higher *Ra* and lower Hartmann numbers. Sivasankaran *et al* [18] numerically studied the Casson fluid HT in a square cavity with a porous material considering the thermal radiation parameter (*Rd*). It was revealed that the characteristics of HT improve by raising the Caisson fluid parameter. However, by increasing the thermal radiation parameter, the HT becomes less favorable [19–26].

The present study deals with the fluid flow and heat transfer in porous media. For this purpose, the effects of TiO$_2$–Al$_2$O$_3$ hybrid nanoparticles on these concentrates and processes were investigated on a base fluid containing water and ethylene glycol (50/50). The nanoparticle is calculated with a constant volume fraction of 0.05 and a shape factor of 5.7. Considering the problem conditions, the governing equations comprising momentum, continuity and energy equations were obtained. The similarity solutions were used to transform the resulting partial differential equations (PDEs) into ordinary differential equations (ODEs) describing the flow and energy functions. Then considering the boundary conditions, the problem was solved. The ODEs were solved using the non-commercial software Flex PDE using the finite numerical solution and element discretisation techniques.

2. Problem formulation and numerical approach

Figure 1a displays the geometry of the problem with associated boundary circumstances. The base fluid was water–ethylene glycol (50/50) with TiO$_2$–Al$_2$O$_3$ as the hybrid nanoparticles. Using the non-commercial Flex PDE software, the ODEs were discretised and solved based on the finite element method. The effect of magnetic field, porosity and heat radiation was identified based on the HT rate and fluid flow, thus determining the average Nusselt magnitude.

The momentum, continuity and energy equations are presented as follows [27]:

$$\frac{\partial u}{\partial x} + \frac{\partial v}{\partial y} = 0 \tag{1}$$

$$\frac{\mu_{nf}}{K}u - \sigma_{hnf}B_0^2\left[v(\sin\gamma)(\cos\gamma) - u(\sin\gamma)^2\right] = -\frac{\partial p}{\partial x}, \tag{2}$$

$$\frac{\mu_{nf}}{K}v - \sigma_{hnf}B_0^2\left[u(\sin\gamma)(\cos\gamma) - v(\cos\gamma)^2\right]$$
$$= -\frac{\partial p}{\partial x} + g(\rho\beta)_{hnf}(T - T_c), \tag{3}$$

$$\frac{1}{\varepsilon}\left[(\rho c_p)_{hnf}^{-1}\frac{\partial q_r}{\partial y} + \left(u\frac{\partial T}{\partial x} + v\frac{\partial T}{\partial y}\right)\right]$$
$$= k_{hnf}\left(\frac{\partial^2 T}{\partial x^2} + \frac{\partial^2 T}{\partial y^2}\right)(\rho c_p)_{hnf}^{-1},$$

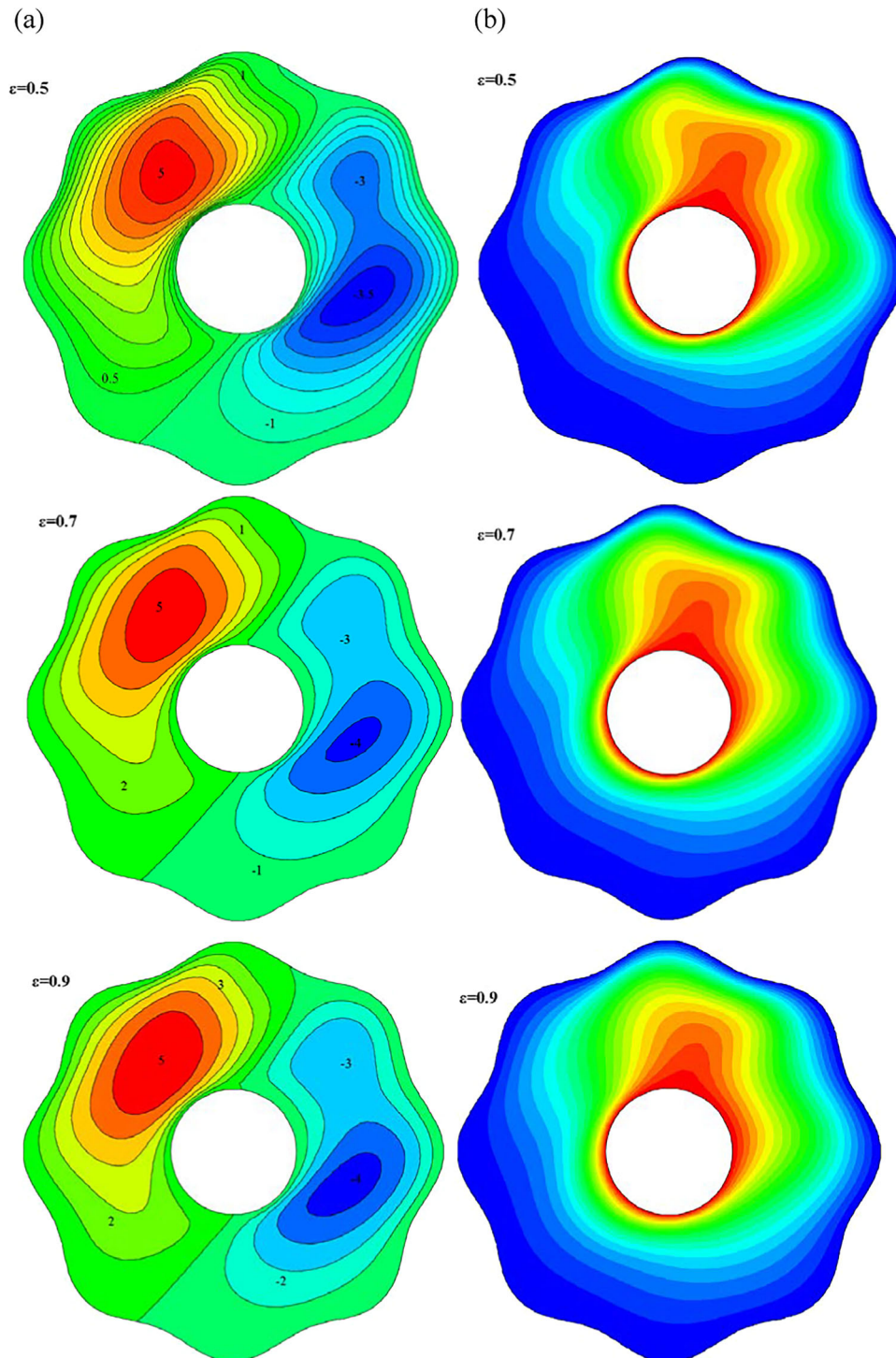(a)   (b)

Figure 3. (**a**) The streamlines and (**b**) isotherms for $\varepsilon = 0.5$, 0.7 and 0.9.

$$q_r = -\left(\frac{4\sigma_e}{3\beta_r}\right)\left(\frac{\partial T^4}{\partial y}\right), \quad T^4 \cong -3T_c^4 + 4T_c^3 T. \quad (4)$$

Here, β is the thermal expansion coefficient, K is the permeability, σ_e is the electrical conductivity, ε is the

porosity of the medium, ρ is the density and q_r is the radiative heat flux.

The formulation for hybrid nanoparticles is also presented below [27]. The hybrid nanofluid (*hnf*) viscosity and thermal conductivity are given in eqs (9) and (10) [28]:
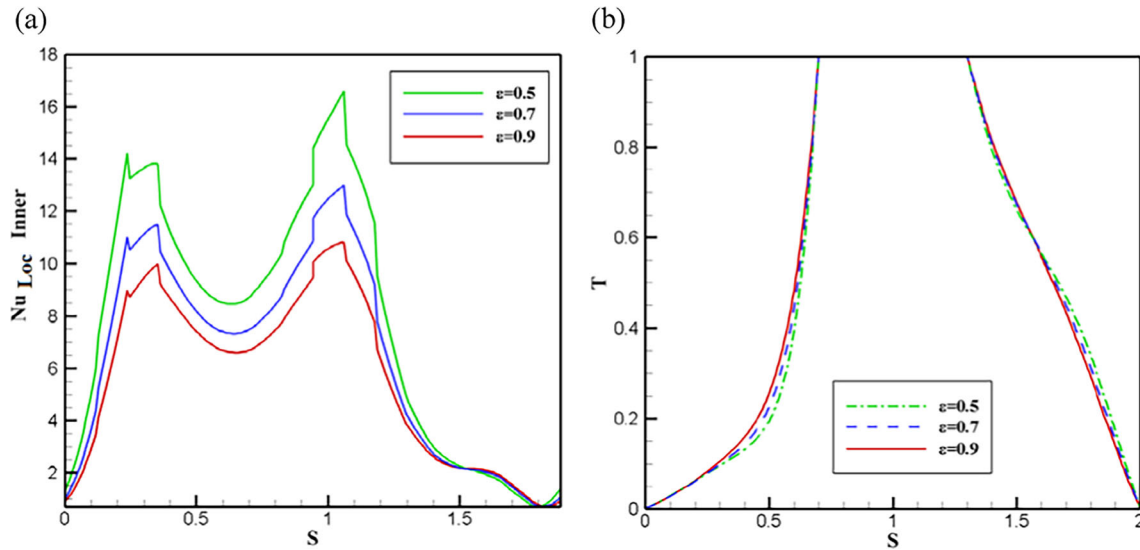
(a)

(b)

Figure 4. (a) The Nu_{Loc} plot and (b) the temperature plot for $\varepsilon = 0.5, 0.7$ and 0.9.

$$\rho_{hnf} = \rho_f(1-\phi_2)\left[(1-\phi_1)+\phi_1\left(\frac{\rho_{s_1}}{\rho_f}\right)\right]+\phi_2\rho_{s_2},$$

(5)

$$(\rho\beta)_{hnf} = (\rho\beta)_f(1-\phi_2)\left[(1-\phi_1)+\phi_1\left(\frac{(\rho\beta)_{s_1}}{(\rho\beta)_f}\right)\right]$$
$$+\phi_2(\rho\beta)_{s_2},$$

(6)

$$(\rho c_p)_{hnf} = (\rho c_p)_f(1-\phi_2)\left[(1-\phi_1)+\phi_1\left(\frac{(\rho c_p)_{s_1}}{(\rho c_p)_f}\right)\right]$$
$$+\phi_2(\rho c_p)_{s_2},$$

(7)

$$\frac{\sigma_{hnf}}{\sigma_{bf}} = 1 + \frac{3\phi[\sigma_1\phi_1 + \sigma_2\phi_2 - \sigma_{bf}(\phi_1+\phi_2)]}{[(\sigma_1\phi_1 + \sigma_2\phi_2 + 2\phi\sigma_{bf}) - \phi\sigma_{bf}((\sigma_1\phi_1 + \sigma_2\phi_2) - \sigma_{bf}(\phi_1+\phi_2))]},$$

(8)

$$\frac{k_{hnf}}{k_{bf}} = \frac{k_{s_2} + (s-1)k_{bf} - (s-1)\phi_2(k_{bf} - k_{s_2})}{k_{s_2} + (s-1)k_{bf} + \phi_2(k_{bf} - k_{s_2})},$$

$$\frac{k_{bf}}{k_f} = \frac{k_{s_1} + (s-1)k_f - (s-1)\phi_1(k_f - k_{s_1})}{k_{s_1} + (s-1)k_f + \phi_1(k_f - k_{s_1})},$$

(9)

$$\mu_{hnf} = \frac{\mu_f}{(1-\phi_1)^{2.5}(1-\phi_2)^{2.5}}.$$

(10)

Here, ϕ is the nanoparticle volume fraction, μ is the dynamic viscosity, c_p is the specific heat capacity, s_1 is the first solid nanoparticle, s_2 is the second solid nanoparticle and k is the thermal conductivity.

The thermo-physical properties of the nanoparticles and base fluid are shown in table 1 [29,30].

Equation (11) displays the dimensionless parameters and stream function (Ψ).

$$v = -\frac{\partial\psi}{\partial x}, \quad u = \frac{\partial\psi}{\partial y}, \quad \Delta T = \frac{Lq''}{k_f},$$

$$\theta = \frac{(T-T_c)}{\Delta T}, \quad (X, Y) = \frac{(x, y)}{L}, \quad \Psi = \frac{\psi}{\alpha_{nf}}.$$

(11)

Here, θ, X and Y correspond to the dimensionless temperature and Cartesian coordinates, respectively.

Equations (12) and (13) represent the concluding terms for the governing equations. The considered constant parameters are described by eq. (14). Furthermore, the conditions for inner and outer walls are obtained by eq. (15) [27].

$$\frac{\partial^2\Psi}{\partial X^2} + \frac{\partial^2\Psi}{\partial Y^2}$$
$$= -\frac{A_6}{A_5}Ha\left[\frac{\partial^2\Psi}{\partial Y^2}(\sin^2\gamma) + \frac{\partial^2\Psi}{\partial X^2}(\cos^2\gamma)\right.$$
$$\left. + 2\frac{\partial^2\Psi}{\partial X\partial Y}(\sin\gamma)(\cos\gamma)\right] - \frac{A_3A_2}{A_4A_5}\frac{\partial\theta}{\partial X}Ra,$$

(12)

$$\varepsilon\left[\left(\frac{\partial^2\theta}{\partial X^2}\right) + \left(1 + \frac{4}{3}\left(\frac{k_f}{k_{hnf}}\right)Rd\right)\left(\frac{\partial^2\theta}{\partial Y^2}\right)\right]$$
$$= -\frac{\partial\theta}{\partial X}\frac{\partial\Psi}{\partial X} + \frac{\partial\Psi}{\partial Y}\frac{\partial\theta}{\partial X},$$

(13)

$$A_1 = \frac{\rho_{hnf}}{\rho_f}, \quad A_2 = \frac{(\rho c_p)_{hnf}}{(\rho c_p)_f}, \quad A_3 = \frac{(\rho\beta)_{hnf}}{(\rho\beta)_f},$$

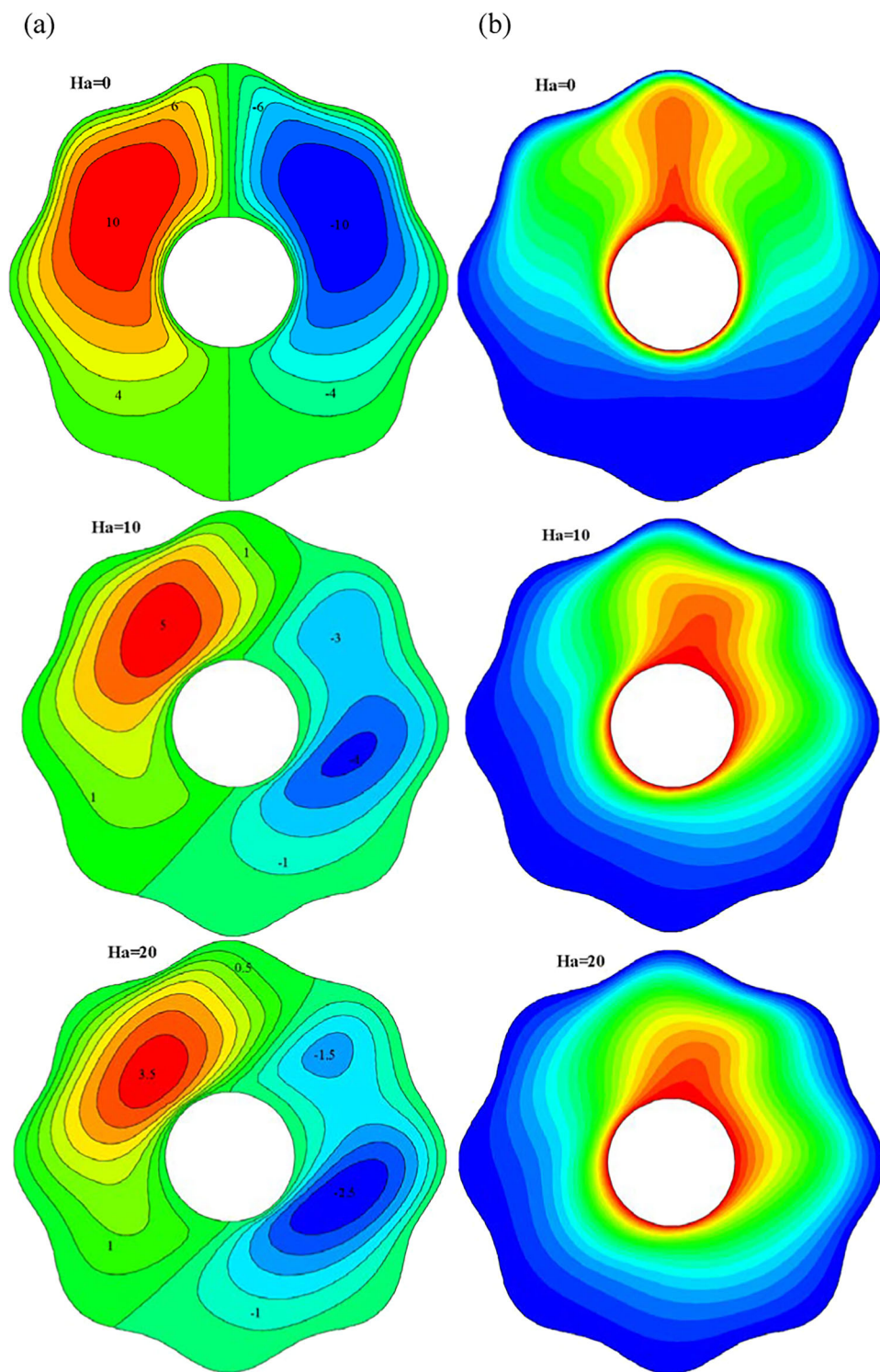(a)   (b)

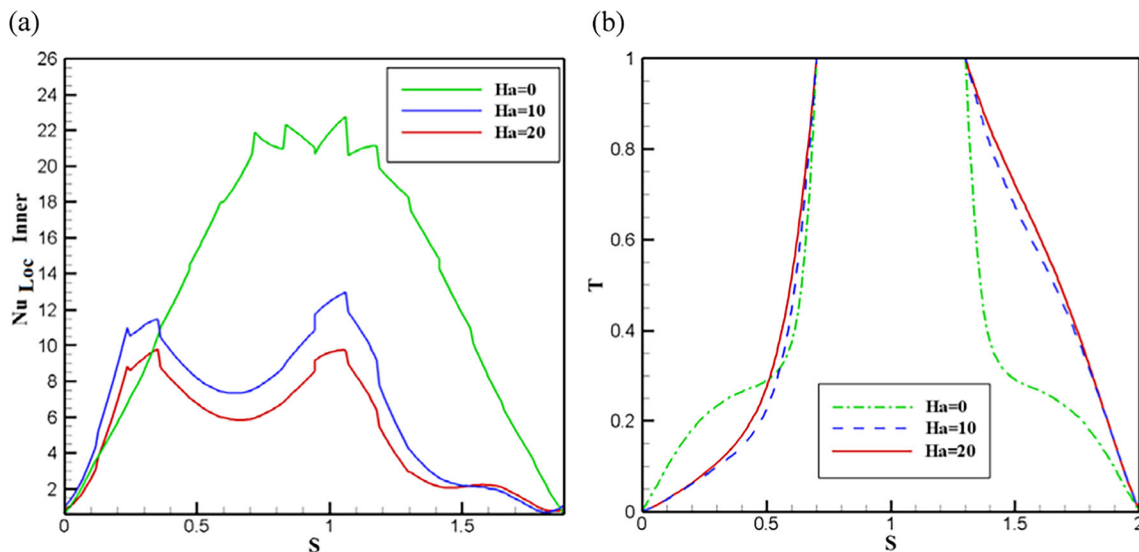**Figure 5.** (**a**) The streamlines and (**b**) isotherms for *Ha* = 0, 10 and 20.

(a)

(b)

Figure 6. (**a**) The Nu_{Loc} plot and (**b**) the temperature plot for $Ha = 0$, 10 and 20.

$$A_4 = \frac{k_{hnf}}{k_f}, \quad A_5 = \frac{\mu_{hnf}}{\mu_f}, \quad A_6 = \frac{\sigma_{hnf}}{\sigma_f},$$

$$Ra = \left(\frac{gK(\rho\beta)_f}{\mu_f\alpha_f}\right)L\Delta T, \quad Ha = \frac{\sigma_f K B_0^2}{\mu_f},$$

$$\delta_s = \frac{k_{hnf}}{[k_s(1-\varepsilon)]}, \tag{14}$$

$$\Psi = 0.0, \quad \text{on all the walls}$$
$$\theta_{nf} = \theta_s = 0.0, \quad \text{on the outer wall} \tag{15}$$
$$\theta_{nf} = \theta_s = 1.0, \quad \text{on the inner wall.}$$

The local (Loc) and average Nusselt numbers are obtained as

$$Nu_{\text{Loc}} = \left(\frac{k_{hnf}}{k_f}\right)\left(\frac{1}{\theta}\right)\left[1 + \frac{4}{3}Rd\left(\frac{k_{hnf}}{k_f}\right)\right] \tag{16}$$

$$Nu_{\text{av}} = \frac{1}{2\pi}\int_0^{2\pi} Nu_{\text{Loc}}\,\mathrm{d}r. \tag{17}$$

Here, δ_s, x and y correspond to the modified thermal conductivity ratio and Cartesian coordinates, respectively.

Nu_{Loc} is calculated on the surface of the geometry (S).

FlexPDE is oriented by Galerkin's standard finite element method (GFEM), which works with linear or cubical second-order interpolation among the quadrilaterals and triangles. To reach accurate meshing and target accuracy, the software continually calculates the solution error thus refining the meshing structure.

3. Grid independence testing, meshing and validation

Figure 1b shows the final modified meshing. As can be seen, meshing is more adaptive in the edge zones. The validity of final unstructured and adaptive meshing was proved by the grid independence test. The grid analysis is shown in figure 2a for three various grid sizes. Nu_{Loc} was determined for each grid size. Finally, the grid = 24,966 was utilised to decrease the CPU computation time.

To validate the results, the findings of the survey were compared with those of Khanfar *et al* [31] (figure 2b), with a correct comparative overlap in the Nu_{av} values. Nanofluids are used to promote heat transmission in a two-dimensional cavity and several relevant parameters are examined. A model is created to examine how well nanofluids in a cavity transfer heat while accounting for solid particle dispersion by Khanfar *et al* Consider CuO nanofluid and the percentage of volume fraction is equal to 0.01.

4. Results and discussion

This section deals with the effect of different physical factors on the fluid flow behaviour and HT rate of the nanofluid.

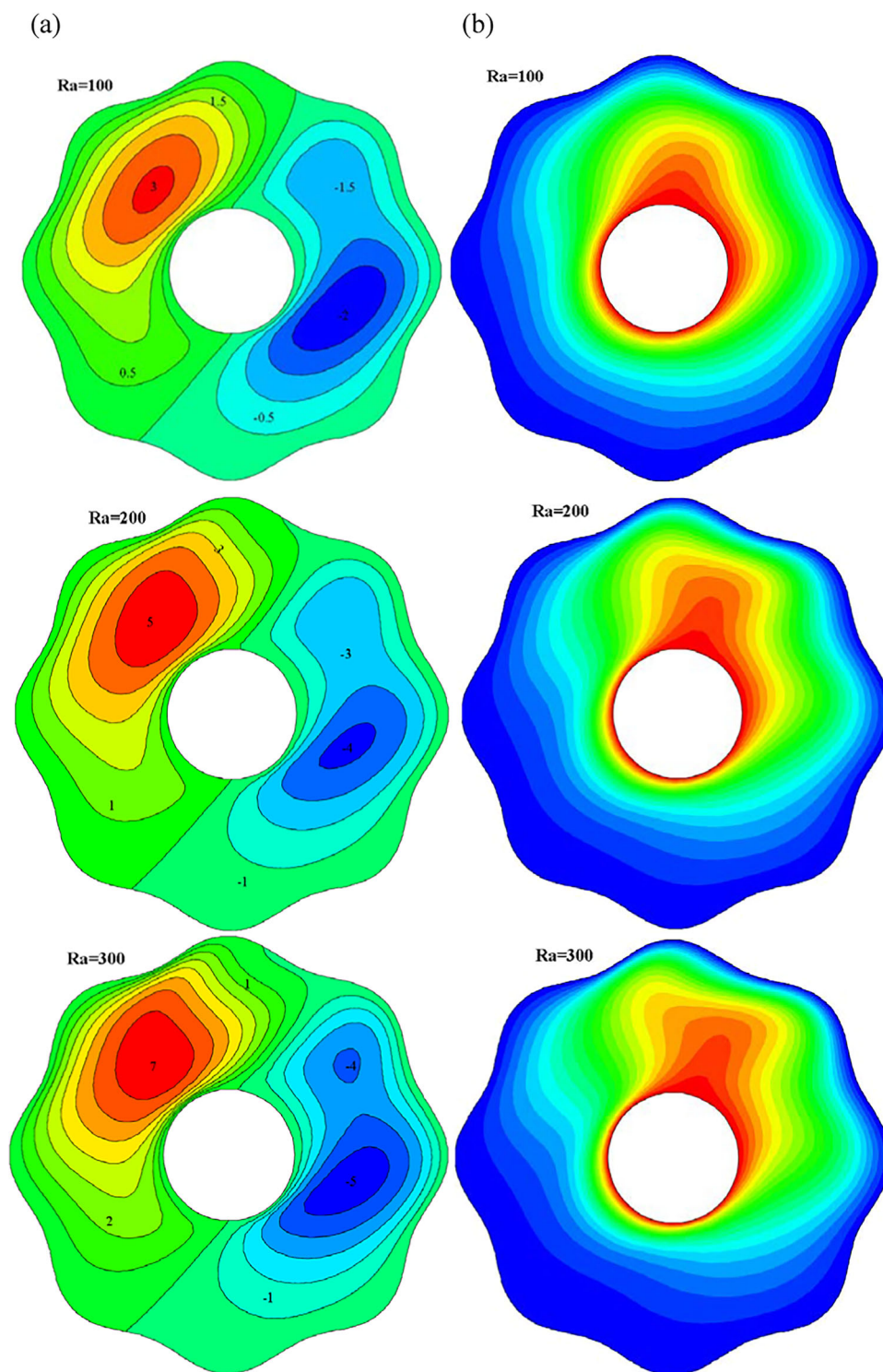The variation of different parameters in this study is shown in table 2.

(a)   (b)

Figure 7. (**a**) The streamlines and (**b**) isotherms for *Ra* = 100, 200 and 300.

(a)

(b)

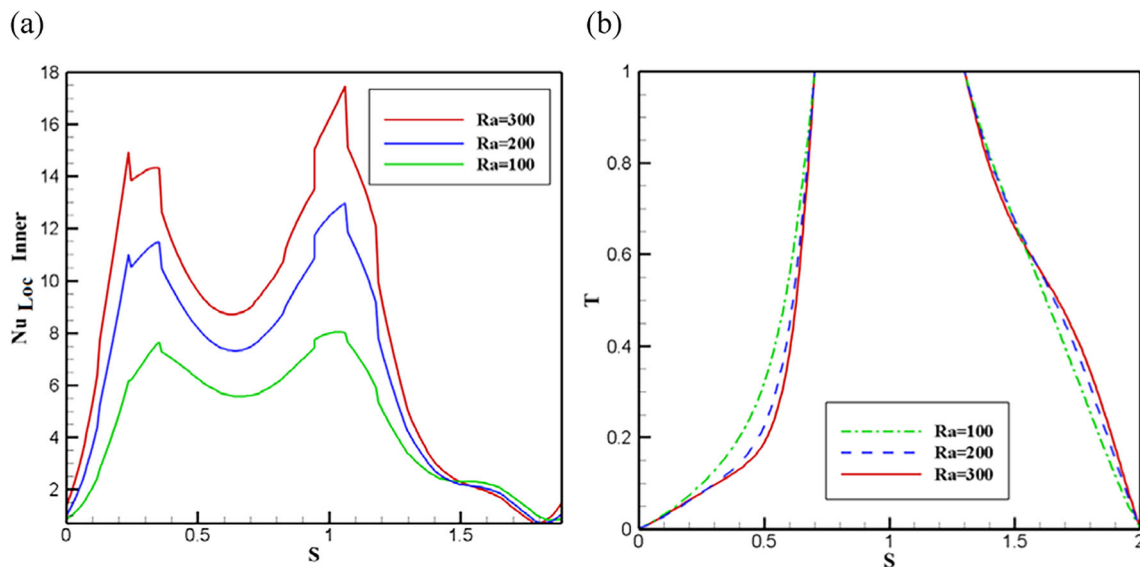**Figure 8.** (**a**) The Nu_{Loc} plot and (**b**) the temperature plot for $Ra = 100$, 200 and 300.

4.1 *Effect of porosity parameter on HT features*

The analysis of streamlines and the isotherm condition is shown in figure 3 for different porosity parameters. The porosity parameters (ε) were chosen as 0.5, 0.7 and 0.9. Moreover, Ra, Rd and Ha are 200, 0.5 and 10, respectively. According to the results, by increasing ε, the temperature is reduced within the cavity. The streamlined contour is also displayed for different sides of the cavity (figure 3). The integrated effects of temperature gradient and gravitational force were obtained for the formation of the vortices. As observed, both the intensity and velocity of the vortices within the cavity are reduced by the increased ε. Besides, by increasing ε, the size of the vortices decreases.

Nu_{Loc} within the cavity concerning different porosities is displayed in figure 4a. As seen, the maximum Nu occurs for porosity $= 0.5$. Thus, the reduced porosity and increased convective flow and the HT rate resulted in a higher Nu. According to the energy equation, an increase in epsilon results in a decrease in the ratio of convective heat transfer to conductive heat transfer, consequently leading to a reduction in Nu. The temperature distribution for various porosities is displayed in figure 4b. It was found that the temperature increased close to the inner wall. Moreover, the increased temperature and ε were directly related.

4.2 *Effect of magnetic field on HT characteristics*

Figure 5 displays the isotherm condition (b) and streamlines (a) for $Ha = 0$, 10 and 20. The values of the ε, Ra and Rd were 0.7, 200 and 0.5, respectively. According

Table 3. The tests designed by the Taguchi method.

Case number	Porosity parameter	Hartman number	Rayleigh number	Radiation parameter
1	0.7	20	100	0.5
2	0.9	10	100	1
3	0.5	20	300	1
4	0.7	10	300	0
5	0.5	10	200	0.5
6	0.5	0	100	0
7	0.7	0	200	1
8	0.9	20	200	0
9	0.9	0	300	0.5

to the results, the absence or existence of the magnetic field results in various flow patterns inside the cavity. Taking into account the streamlines within the cavity, it was found that the strength of the vortices in both the clockwise and counterclockwise directions significantly decreased with increasing magnetic field. Conversely, electric vortices were induced in the current by incrementing the magnetic field resulting in the incremented resistance. Therefore, the HT penetration is reduced from the hot to the cold wall thus reducing HT. The mixture is electrically conductive due to the presence of ions from the hybrid nanofluid that produces electric vortices due to the Lorentz force in the presence of a magnetic field as governed by eqs (2) and (3).

The effect of Ha on Nu_{Loc} is presented in figure 6a. As observed, an inverse relationship exists between HT and
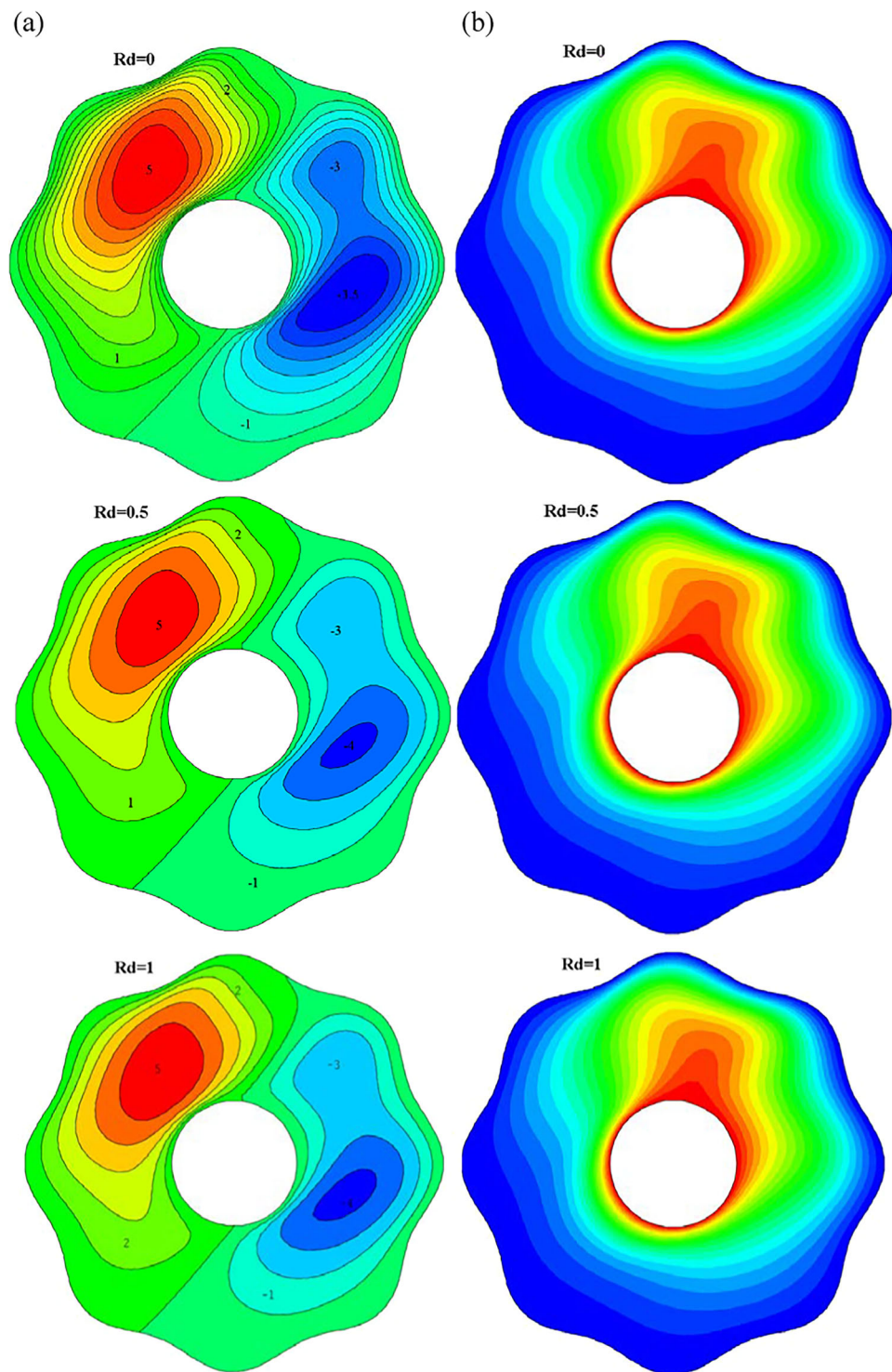
(a)

(b)

Figure 9. (**a**) The streamlines and (**b**) isotherms for *Rd* = 0, 0.5 and 1.

(a)

(b)

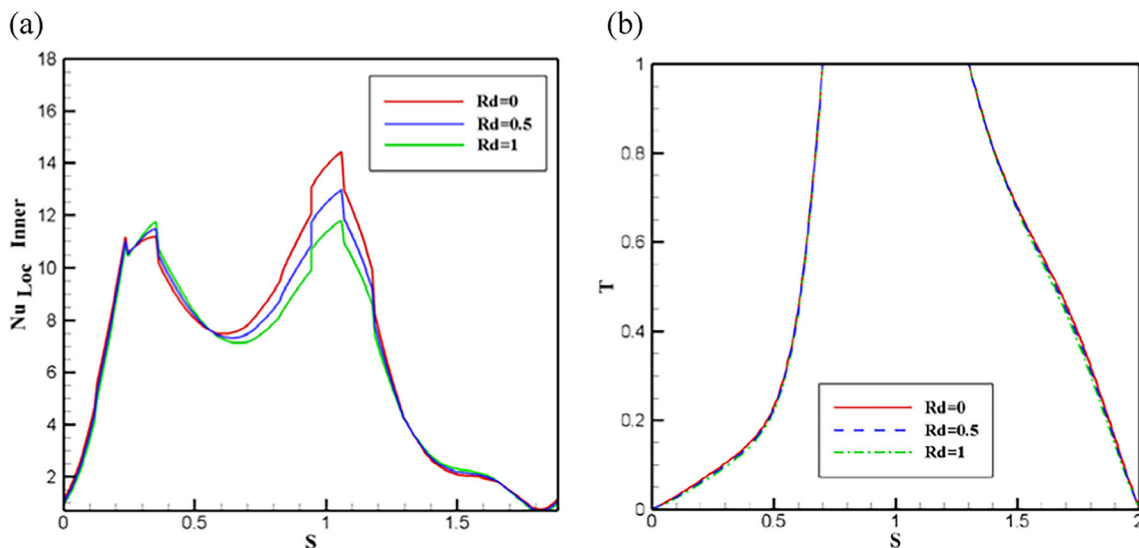**Figure 10.** (**a**) The Nu_{Loc} plot and (**b**) the temperature plot for $Rd = 0$, 0.5 and 1.

Table 4. The variance analysis (ANOVA).

Source	Sum of squares	df	Mean square	F-value	p-value	
Model	379.67	4	94.92	8.90	0.0285	Significant
A-ε	7.00	1	7.00	0.6565	0.4633	
B-Ha	306.45	1	306.45	28.75	0.0058	
C-Ra	66.13	1	66.13	6.20	0.0674	
D-Rd	0.0840	1	0.0840	0.0079	0.9335	
$R^2 = 0.899$						

Ha owing to Lorentz forces and electrical vortices resisting the convective flow. Therefore, Nu_{Loc} is reduced by increasing Ha. Figure 6b shows the temperature distribution for different values of Ha. According to the acquired data, without a magnetic field, a completely different temperature profile was developed. As the intensity of the magnetic field increases due to increased friction work, the temperature profile increases.

4.3 *Effects of Ra on the HT characteristics*

Figure 7 represents the streamlines (a) and isotherm condition (b) for $Ra = 100$, 200 and 300. Here, ε, Ha and Rd are 0.7, 10 and 0.5, respectively. It is worth stating that Ra is the ratio of the thermal diffusivity to the buoyancy force. Therefore, the effect of buoyancy forces is negligible at low Ra and HT is associated with higher conductivity. According to figure 7, by increasing Ra, both fluid flow and molecular motion increase. Based on the streamlines, the value of the stream function significantly increases at the centre of the vortices by
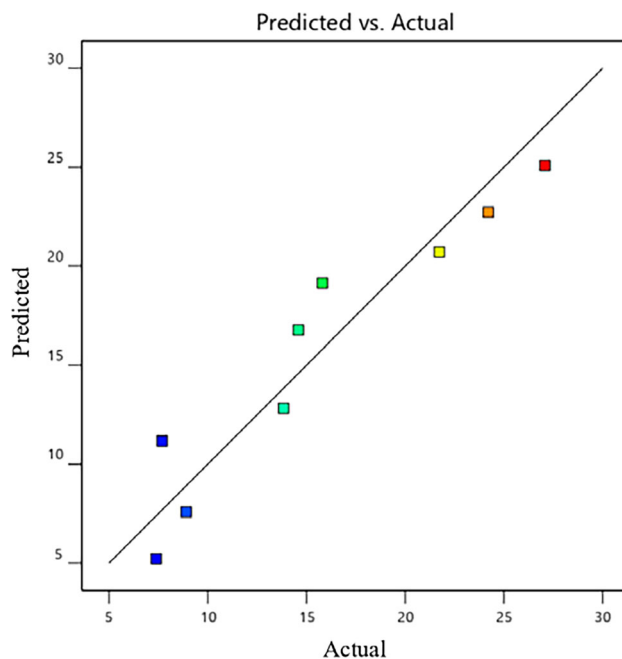

Figure 11. The predicted vs. actual of Nu_{av}.

Table 5. The outcome of the optimisation procedure by RSM.

Parameter	Optimum value
ε	0.52
Ha	0.1
Ra	299.4
Rd	0.133

the increased Ra. The stream function is maximum at $Ra = 300$. The vortex strength and the chamber fluid flow velocity are incremented by the increase in buoyancy force in this situation.

As seen in figure 8a, the HT rate is improved by the augmentation of Ra as well as the increased buoyancy forces. Thus, Nu_{Loc} is also incremented. Figure 8b shows the temperature distribution for various Ra. From the findings, it can be seen that the temperature graph's curvature grows as Ra rises. Furthermore, the irregularity increases with the increased Ra, thus increasing the HT rate.

4.4 *Effect of radiation parameter on HT features*

Figure 9 represents the isotherm condition (b) and streamlines (a) based on different values of Rd (0, 0.5 and 1). The Ha, porosity parameter and Ra for the simulation in this part were 0.7, 10 and 200, respectively. According to the results, without Rd, the streamlines appear to be denser. However, they have comparatively lower intensity. Moreover, the results revealed that for all three Rd values, the temperature profile increases.

The Nu_{Loc} for different radiation settings is shown in figure 10a. HT is reduced by augmentation of this parameter owing to radiant energy losses thus decrementing Nu_{Loc}. The temperature distribution for various values of Rd is shown in figure 10b. According to the results, the temperature profile is less affected by altering Rd.

4.5 *Optimisation, variance analysis and correlation*

As a test design, the Taguchi method is used to achieve a state where the return characteristic tends to have the least fluctuation and the ideal state [32,33]. Generally, based on the intended objective, three definable and desirable design features in the Taguchi technique include the highest, the nominal value and the lowest values. Rd, Ha, ε and Ra are the considered variables. Table 3 presents the information on the included variables. It should be noted that the number of tests was reduced from 81 to 9 using the Taguchi approach.

The problem is modelled by response surface methodology (RSM) as an optimisation technique, through a set of statistical and mathematical methods. The reduced calculation cost is one of the benefits of this technique. First, this method was utilised for laboratory data, which was later expanded for modelling and numerical research. The two approaches are different based on the type of errors. This method highly required a correlation to assess the effects of variable parameters on the objective function. The general quadratic polynomial relation in RSM is as follows:

$$y = a_0 + \sum_{i=1}^{n} a_i x_i + \sum_{i=1}^{n} a_{ii} x_i^2 + \sum_{i=1}^{n} \sum_{j=1}^{n} a_{ij} x_i x_j + \xi,$$
$$i < j. \tag{18}$$

- The predicted response, linear, constant and quadratic coefficient and interaction factor are defined as y, a_i, a_0, a_{ii} and a_{ij}.
- The error is represented by the design parameters described as x_i, x_j and ξ.

The examination of parameters in the prediction regression utilising variance analysis (ANOVA) is shown in table 4. ANOVA helps to comprehend and assess the discrepancy scale of the actual results and estimated outcomes. In the present work, a proper overlap is shown by this differentiation between real results and predicted outcomes with the R-squared value of 89.9% (figure 11).

For this purpose, the maximum Nu_{av} in the obtained correlation is

$$Nu_{av} = 20.099 - 5.04(\varepsilon) - 0.714(Ha) + 0.033(Ra) - 0.236(Rd). \tag{19}$$

The optimum values for the operating variables in the correlation are listed in table 5, which results in the maximum Nu.

Figure 11 shows the actual and predicted values for the Nu_{av} relative to the hypothetical line.

The combined effect of the involved operating factors on Nu is also shown in figure 12.

These values are presented using the response surface technique. As observed, the Nu increases as Ra increases. It should be noted that Nu_{av} decreases as Ha, Rd and ε increase.

5. Conclusions

In the present paper, the fluid flow and HT in a porous medium were numerically examined. An investigation was also performed on the effect of thermal
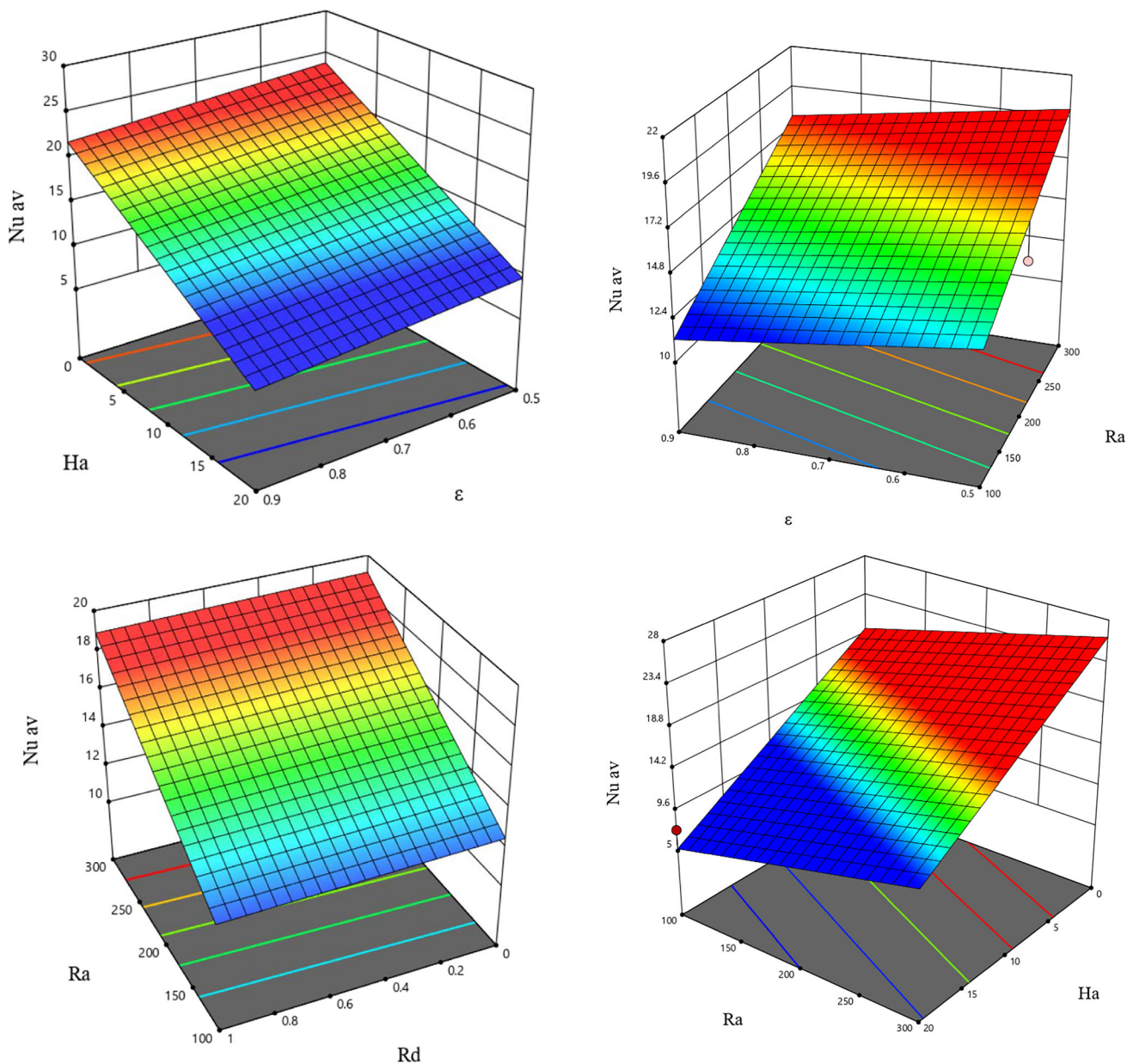
Figure 12. The effects of various operating parameters on Nu_{av} by RSM

radiation field, porosity and magnetic parameters on the flow pattern and HT rate. Moreover, using the appropriate correlations, Nu_{av} was determined. Using the RSM, the optimal values were also determined. Mainly, in the present work, the following findings were obtained:

- The velocity and strength of the vortices within the cavity are reduced by increasing ε. Moreover, by raising the porosity value, the size of the vortices is reduced.
- The increased Ha significantly amplifies the intensity of the vortices.

- The co-flowing streamlines and HT rate are caused by the higher Ha owing to Lorentz forces and resistance from vortices induced electrically. Thus, Nu_{Loc} is decreased by incrementing the Ha.
- The HT by convection is improved with an increased Ra, associated with the intensified buoyancy forces. Therefore, Nu_{Loc} correspondingly increases.
- For Nu_{av}, the optimal values are $\varepsilon = 0.52$, $Ra = 299.4$, $Ha = 1.0$ and $Rd = 0.133$.

In future, the influence of other parameters on vortex dynamics and heat transfer may be studied and the experimental validation of the numerical results is important.

References

[1] K Walker and G M Homsy, *J. Fluid Mech.* **87**, 449 (1978)

[2] A K Hussein and A W Mustafa, *Therm. Sci. Eng. Prog.* **1**, 66 (2017)

[3] S Parvin and A Akter, *Proc. Eng.* **194**, 421 (2017)

[4] C Sivaraj and M A Sheremet, *J. Magn. Magn. Mater.* **426**, 351 (2017)

[5] S Y Motlagh and H Soltanipour, *Int. J. Therm. Sci.* **111**, 310 (2017)

[6] K Janagi, S Sivasankaran, M Bhuvaneswari and M Eswaramurthi, *Int. J. Numer. Methods Heat Fluid Flow* **27**, 1000 (2017)

[7] A Abedini, T Armaghani and A J Chamkha, *J. Therm. Anal. Calorim.* **135**, 685 (2018)

[8] A Hassanpour, A A Ranjbar and M Sheikholeslami, *Eur. Phys. J. Plus.* **133**, 66 (2018)

[9] A Rashad, Taher Armaghani, A J Chamkha and M A Mansour, *Chin. J. Phys.* **56**, 193 (2018)

[10] M Salari, E H Malekshah and M H Malekshah, *Alex. Eng. J.* **57**, 1401 (2018)

[11] S E Ahmed, M A Mansour, A Rashad and T Salah, *J. Therm. Anal. Calorim.* **139**, 3133 (2020)

[12] A A Alnaqi, S Aghakhani, A H Pordanjani, R Bakhtiari, A Asadi and M D Tran, *Int. J. Heat Mass Transfer* **133**, 256 (2019).

[13] Q Yu, Y Lu, C Zhang, Y Wu and B Sunden, *J. Therm. Anal. Calorim.* **141**, 1207 (2019)

[14] A S Dogonchi, M K Nayak, N Karimi, A J Chamkha and D D Ganji, *J. Therm. Anal. Calorim.* **141**, 2109 (2020)

[15] B P Geridonmez and H F Oztop, *Comput. Math. Appl.* **80**, 2796 (2020)

[16] A S Dogonchi, A J Chamkha and D D Ganji, *J. Therm. Anal. Calorim.* **135**, 2599 (2018)

[17] M S Sadeghi, T Tayebi, A S Dogonchi, T Armaghani and P Talebizadehsardari, *Math. Methods Appl. Sci.* (2020), https://doi.org/10.1002/mma.6520

[18] S Sivasankaran, M Bhuvaneswari and A K Alzahrani, *Alex. Eng. J.* **59**, 3315 (2020)

[19] W Ibrahim and M Hirpho, *Heliyon.* **7**, e07683 (2021)

[20] A Jarray, Z Mehrez and A E Cafsi, *Pramana – J. Phys.* **94**, 156 (2020)

[21] H Ouri, F Selimefendigil, M Bouterra, M Omri, B M Alshammari and L Kolsi, *Alex. Eng. J.* **63**, 563 (2023)

[22] H A Nabwey, A M Rashad, P Bala, S Jakeer, M A Mansour and T Salah, *Alex. Eng. J.* **65**, 921 (2023)

[23] N Alipour, B Jafari and Kh Hosseinzadeh, *Heliyon.* **9**, e22257 (2023)

[24] Kh Hosseinzadeh, M Roshani, M A Attar, D D Ganji and M B Shafii, *Heliyon.* **9**, e20193 (2023)

[25] Kh Hosseinzadeh, S Akbari, S Faghiri and M B Shafii, *Int. J. Thermofluids* **18**, 100337 (2023)

[26] N Alipour, B Jafari and K Hosseinzadeh, *Sci. Rep.* **13**, 1635 (2023)

[27] Kh Hosseinzadeh, A Asadi, A R Mogharrebi and M E Azari, *J. Therm. Anal. Calorim.* **143**, 1081 (2020)

[28] Kh Hosseinzadeh, S Roghani, A Asadi, A Mogharrebi and D D Ganji, *Int. J. Numer. Meth. Heat Fluid Flow* **31**, 402 (2020)

[29] Kh Hosseinzadeh, A R Mogharrebi, A Asadi, M Paikar and D D Ganji, *J. Mol. Liq.* **300**, 112347 (2020)

[30] Kh Hosseinzadeh, D D Ganji, M A E Moghaddam, A Asadi and A R Mogharrebi, *Renew. Energy* **154,** 497 (2020)

[31] K Khanafer, K Vafai and M Lightstone, *Int. J. Heat Mass Transfer.* **46**, 3639 (2003)

[32] G Taguchi, *Introduction to quality engineering designing quality into products and processes* (Tokyo Asian Productivity Organization, 1990)

[33] G Taguchi and G Taguchi, *Introduction to quality engineering* (Asian Productivity Organization) (1986)